

A MEMS platform for *in situ*, real-time monitoring of electrochemically induced mechanical changes in lithium-ion battery electrodes

This content has been downloaded from IOPscience. Please scroll down to see the full text.

2013 J. Micromech. Microeng. 23 114018

(<http://iopscience.iop.org/0960-1317/23/11/114018>)

View [the table of contents for this issue](#), or go to the [journal homepage](#) for more

Download details:

IP Address: 129.2.129.155

This content was downloaded on 15/01/2014 at 14:15

Please note that [terms and conditions apply](#).

A MEMS platform for *in situ*, real-time monitoring of electrochemically induced mechanical changes in lithium-ion battery electrodes

Ekaterina Pomerantseva¹, Hyun Jung¹, Markus Gnerlich¹, Sergio Baron¹, Konstantinos Gerasopoulos^{1,2} and Reza Ghodssi^{1,2}

¹ MEMS Sensors and Actuators Laboratory (MSAL), Department of Electrical and Computer Engineering, Institute for Systems Research, University of Maryland, College Park, MD 20742, USA

² Department of Materials Science and Engineering, University of Maryland, College Park, MD 20742, USA

E-mail: ghodssi@umd.edu

Received 29 March 2013, in final form 3 September 2013

Published 25 October 2013

Online at stacks.iop.org/JMM/23/114018

Abstract

We report the first successful demonstration of an optical microelectromechanical systems (MEMS) sensing platform for the *in situ* characterization of electrochemically induced reversible mechanical changes in lithium-ion battery (LIB) electrodes. The platform consists of an array of flexible membranes with a reflective surface on one side and a thin-film LIB electrode on the other side. The membranes deflect due to the active battery material volume change caused by lithium intercalation (expansion) and extraction (contraction). This deflection is monitored using the Fabry–Perot optical interferometry principle. The active material volume change causes high internal stresses and mechanical degradation of the electrodes. The stress evolution observed in a silicon thin-film electrode incorporated into this MEMS platform follows a ‘first elastic, then plastic’ deformation scheme. Understanding of the internal stresses in battery electrodes during discharge/charge is important for improving the reliability and cycle lifetime of LIBs. The developed MEMS platform presents a new method for *in situ* diagnostics of thin-film LIB electrodes to aid the development of new materials, optimization of electrode performance, and prevention of battery failure.

(Some figures may appear in colour only in the online journal)

1. Introduction

Lithium-ion batteries (LIBs) are the most commonly used rechargeable batteries in commercial applications. They offer high energy density compared to other battery systems while also being compact and lightweight devices [1]. A highly promising class of active LIB materials includes Si, Sn, Sb, Al, Mg, etc. and is referred to as alloying anodes [2, 3]. These materials are characterized by significantly higher theoretical specific capacities compared to the graphite anodes currently used in commercial LIBs. However, these materials generally suffer from a large irreversible capacity loss at the first cycle and poor cycling stability due to the large volume

change during lithium cycling. This leads to high internal stress, electrode pulverization and subsequent loss of electrical contact between the active material and current collector, which is accompanied by rapid capacity loss [4, 5]. Stress, generated by lithium intercalation, has been considered as a major factor related to the degradation of alloying anodes. Post-operational destructive examination of the electrodes can provide useful information. For example, depth-sensing indentation experiments enabled *ex situ* measurements of the Young’s modulus and hardness of thin-film silicon electrodes at various stages of lithium intercalation [6]. However, *in situ* stress transition in such systems caused by lithium intercalation/extraction is not well understood. New *in situ*

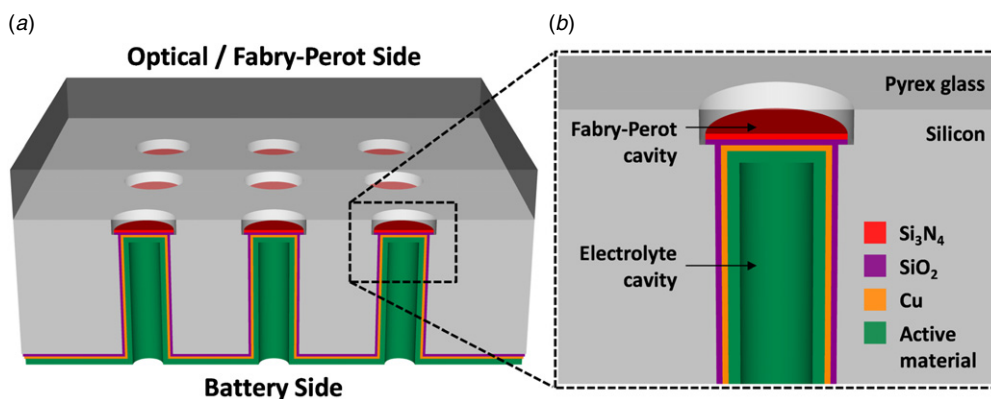


Figure 1. (a) 3D and (b) cross-section diagrams of the MEMS sensing platform design.

materials characterization tools are needed to understand how materials change during each cycle inside a battery to improve battery life.

The multi-beam optical sensor (MOS) technique has proven to be an effective method for *in situ* measurements of mechanical properties in silicon thin-film electrodes during lithium cycling [7–13]. In MOS, the sample wafer is coated with a silicon oxide barrier layer, copper current collector and thin-film silicon active electrode. This stack is assembled into an electrochemical cell. An array of parallel laser beams is shone on the sample wafer surface. The stress generated in the silicon film due to lithium intercalation causes bending of the wafer. The wafer curvature is determined by measuring the relative change in the spacing between the reflected beams and used to calculate mechanical properties of the silicon electrode. It was shown that upon lithium intercalation, due to substrate constraints, the silicon electrode initially undergoes elastic deformation, resulting in rapid rise of compressive stress. Afterwards, the electrode begins to deform plastically, and subsequent lithium insertion results in continued plastic strain. During charge (lithium extraction), the electrode first undergoes elastic straining in the opposite direction. Subsequently, it deforms plastically during the rest of charge [8]. The existence of the stress–potential coupling in lithiated silicon was inferred by analysis of experimental results combined with calculations [10]. Using the same technique the authors measured *in situ* stress and biaxial moduli of a silicon thin-film electrode as a function of the lithium concentration [9]. Evolution of in-plane stresses in amorphous silicon films with different thickness (from 50 to 250 nm), investigated using the *in situ* MOS technique, revealed decrease in both nominal flow stress and the specific capacity of electrodes, which was related to slow lithium diffusion [12]. The effect of diffusion limitations was later studied by varying current rates. The results indicated that slow lithium diffusion in silicon films leads to a stress gradient between the lithiated and unlithiated regions. Operation at high current rates was shown to result in large localized stress gradients and film cracking [11, 13].

Despite its high sensitivity, the major disadvantage of the MOS technique is averaging of the measurements over the large wafer-scale area. Thus, the MOS technique works best for samples which are spatially homogeneous over the length scale

of the wafer. Moreover, the MOS technique is not applicable to the study of several materials simultaneously, making it time-consuming for combinatorial materials characterization often required for battery electrode design and optimization. Another disadvantage is that experiments have to be carried out in the inert atmosphere of a glove box. The development of a miniaturized sensing system with similar sensitivity and potential for simultaneous multiple materials monitoring in the ambient environment would be highly desirable.

In this work, we present a new microelectromechanical systems (MEMS) sensing platform for *in situ* monitoring and measurement of changes in mechanical properties of thin-film LIB electrodes using Fabry–Perot interferometry [14]. Here we focus on application-driven design of the platform, its fabrication, packaging and initial characterization. The platform is capable of measuring local phenomena occurring within small 150–300 μm diameter membrane area. It has the potential to be used in combinatorial materials study and can be used for both cathode and anode LIB materials. Adjustment of the membrane geometry, including thickness and diameter, enables simple tuning of the sensitivity so that materials with smaller volume expansion can be studied with the same platform and fabrication methods. This work highlights the potential of MEMS technology to enable real-time *in situ* characterization of materials combined with improved reliability and higher sensitivity in the ambient environment.

2. Design and fabrication

The MEMS sensing platform consists of an array of mechanically responsive flexible silicon nitride membranes (figure 1). The membranes are separated by a gap from a Pyrex wafer. During operation, a red laser light illuminates the Fabry–Perot cavity. The light reflects from the membrane and Pyrex glass surfaces producing a Fabry–Perot interference pattern. On the other side of the membrane there is another deep cavity coated with the battery electrode materials. The membrane separates two sides of the platform, referred to as the ‘Fabry–Perot’ and ‘battery’ sides. Unique to this design, optical and electrochemical measurements are decoupled allowing *in situ* experiments with air-sensitive lithium-ion chemistry. The ‘battery’ side of the platform is coated with several

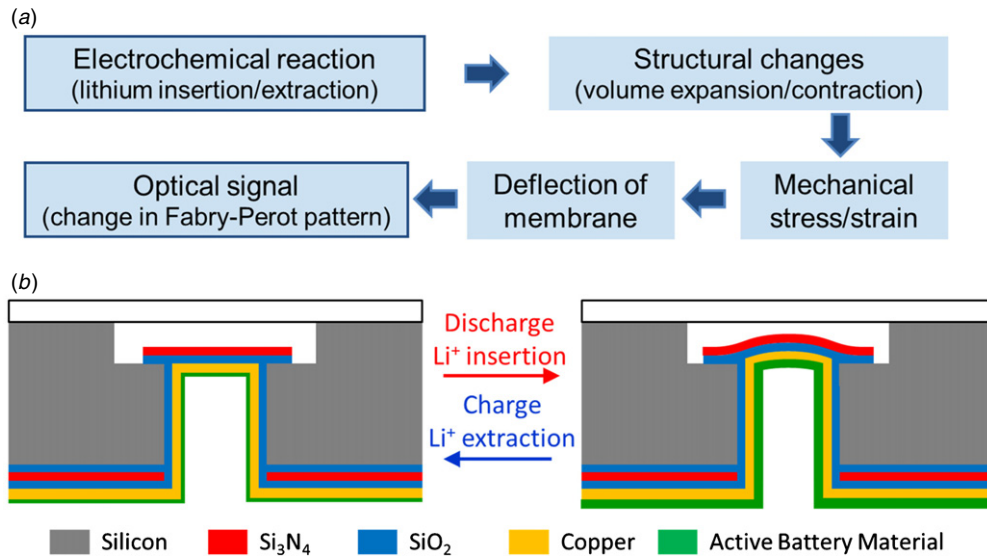


Figure 2. Schematic presentations of (a) MEMS sensing platform operation and (b) cross-section diagram of the principle behind the sensing mechanism of the platform. Monochromatic light is shone through the top to create optical interference in the ‘Fabry–Perot’ cavity, which is observable as a set of light and dark fringes.

materials, each playing a particular role in the operation of device. First, a silicon oxide layer is deposited that blocks lithium intercalation into the bulk silicon wafer. The following metal layer (Ti/Cu/Ti) serves as a current collector. The top layer is silicon which acts as the active battery material in the electrochemical experiments.

The principle of operation of the platform is shown in figure 2. During discharge, lithium intercalation causes volume expansion of the active battery material. This induces stress and deflection of the flexible silicon nitride membrane, which in turn changes the distance between the membrane and Pyrex glass monitored optically by observing change in the Fabry–Perot pattern. On charge, the processes are reversed and the membrane deflects back to its original state.

According to the literature [12], the maximum nominal stress (σ_{nom}) that resides in a 50 nm thin-film silicon electrode during electrochemical cycling is 1.55 GPa (this corresponds to the fully lithiated silicon). Using this maximum stress information, the maximum expected membrane deflection was calculated, which defined our choice of the Fabry–Perot cavity depth. Under the simplified assumption that the membrane is a uniform Si_3N_4 layer with $1.0 \mu\text{m}$ thickness, membrane deflection due to residual stress should follow the behavior of a circular thin plate with clamped edge under uniform loading [15]. The deflection of the membrane (W) along the membrane diameter (r) is described by equation (1), where q_0 is the applied pressure, a is the radius of the membrane, D is the flexural rigidity (equation (2)), E is the Young’s modulus, and ν is Poisson’s ratio:

$$W(r) = \frac{q_0}{64D} (a^2 - r^2)^2 \quad (1)$$

$$D = \frac{Eh^3}{12(1 - \nu^2)} \quad (2)$$

The maximum stress that the electrode experiences during the electrochemical reaction is of primary interest. The stress

Table 1. Parameters used for evaluation of Fabry–Perot cavity depth.

Parameter	Value
Applied pressure (q_0)	93.867 kPa
Radius of the membrane (a)	75 or 100 μm
Thickness of the Si_3N_4 membrane (h)	1 μm
Flexural rigidity (D) [14]	$2.65 \times 10^{-8} \text{ Pa} \cdot \text{m}^3$

residing in the membrane is shown in equation (3), where z is the position along the z -axis, h is the thickness of the membrane and ν is the Poisson’s ratio

$$\sigma_{rr}(r, z) = \frac{3q_0a^2z}{4h^3} \left[(1 + \nu) - (3 + \nu) \frac{r^2}{a^2} \right] \quad (3)$$

The maximum stress occurs at the bottom surface of the membrane (where r is equal to a and z is equal to $-h/2$) and is defined by equation (4):

$$q_0 = \frac{\sigma_{rr}(a, -h/2)4h^2}{3a^2} \quad (4)$$

If the maximum nominal stress value (1.55 GPa) is substituted into equation (4), the corresponding pressure can be found. According to this calculation, the maximum induced deflection of the membrane is $6.85 \mu\text{m}$ (when a is 75 μm) and $12.17 \mu\text{m}$ (when a is 100 μm). The parameters used in this simulation are specified in table 1. The total measured thickness of the membrane is $1.4 \mu\text{m}$ (see scanning electron microscope (SEM) images below), and it is thicker than the Si_3N_4 layer thickness (1 μm) used in this analysis. The thicker membrane will result in smaller deflection of the membrane. Therefore, the Fabry–Perot cavity depth (12 μm) used in our design can accommodate the maximum expected stress induced during Li cycling. In addition, devices with wider radius membranes (125 and 150 μm) were included in the layout since wider membranes are more responsive to stress and this can increase the sensitivity of the device.

Figure 3 shows the fabrication process flow for the MEMS platform. Silicon wafers (double-side polished, 100 mm

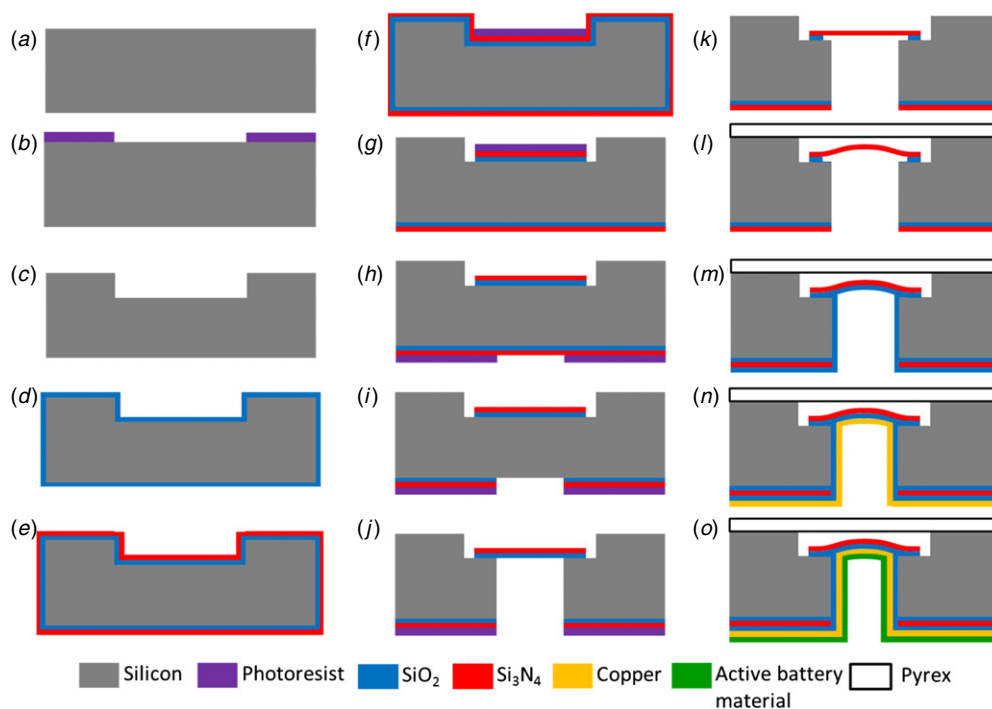


Figure 3. Sensing platform fabrication process flow showing (a) substrate, (b) photoresist etch mask for Fabry–Perot cavity, (c) DRIE, (d) LPCVD SiO₂, (e) LPCVD Si₃N₄, (f) photoresist etch mask for membrane, (g) RIE Si₃N₄ and SiO₂, (h) photoresist mask for backside etch of battery cavity, (i) RIE Si₃N₄ and SiO₂, (j) DRIE, (k) buffered oxide etch of SiO₂, (l) anodic bonding of Pyrex to silicon wafer, (m) PECVD SiO₂, (n) sputtered deposition of Cu current collector, and (o) sputtered deposition of Si.

diameter, nominally 495–505 μm thick, (1 0 0) orientation) were used as substrates. First, 12 μm deep cavities for the Fabry–Perot side were formed by deep reactive-ion etching (DRIE; Surface Technology Systems) on one side of a silicon wafer (figures 3(a)–(c)). The diameter of the Fabry–Perot cavities (150, 200, 250 and 300 μm) defines the diameter of membranes later in the process. With the given membrane thickness, the membranes with larger diameter are expected to demonstrate higher sensitivity, at the same time the membranes with smaller diameter are more mechanically robust. A 300 nm thick layer of SiO₂ is deposited followed by a 700 nm thick layer of Si₃N₄ on both sides of the silicon wafer using low pressure chemical vapor deposition (LPCVD, Tystar Tytan, figures 3(d)–(e)). The silicon nitride is the first layer of the sensing membranes, while the silicon oxide serves as the etch stop for the second DRIE on the ‘battery’ side of the wafer. Then, the Si₃N₄ and SiO₂ are masked with photoresist and etched using reactive-ion etching (RIE; Oxford Plasmalab System 100, Oxford Instruments) from the ‘Fabry–Perot’ side of the platform, leaving the materials in the cavities only (figures 3(f)–(g)). The battery cavities are defined on the ‘battery’ side of the wafer using photoresist (figure 3(g)) and fabricated by successive etching of SiO₂, Si₃N₄ (RIE), and Si (DRIE) (figures 3(h)–(j)). To remove the SiO₂ etch stop layer and release the membranes the platform is immersed in a 5:1 buffered hydrofluoric acid (BOE) for 3 min (figure 3(k)). This also helps to remove any residues and produce a clean surface which is critical for the following step. The silicon and Pyrex wafers are anodically bonded (EVG 501, EV Group, figure 3(l)) followed by dicing of the wafer stack into individual 1 cm \times 1 cm chips. After the bonding, it

is observed that the membranes have an upward curvature. This may be a result of the high compressive stress in the nitride as well as the inevitable annealing that takes place during the bonding process. Finally, the LIB constituents are deposited on the ‘battery’ side of the platform: 200 nm thick SiO₂ (plasma enhanced physical vapor deposition, PECVD, Oxford Plasmalab System 100, Oxford Instruments), 250 nm thick Cu current collector and 500 nm thick Si (sputtering, ATC 1800-V, AJA International) (figures 3(m)–(o)). The Cu current collector was sandwiched between Ti layers (5–20 nm) serving as an adhesion layer between the Cu and SiO₂ and preventing the Cu from oxidizing prior to silicon sputtering. When combined with a Li-conducting electrolyte and metallic lithium as a counter electrode in a coin cell package, this side of the device forms a lithium half-cell or battery system.

When selecting the thickness of the current collector (Cu) and active battery material (Si) the following aspects were considered. First, a thinner Cu layer would result in a thinner membrane, which would provide a more sensitive response, but adequate thickness is needed to ensure conformal coating and adequate electron transport. Electrochemical tests, carried out on planar substrates with different Cu thickness (Si thickness was fixed at 100 nm), demonstrated that the Cu thickness should be at least 15 nm. Cells with the current collector thinner than 15 nm did not show reliable electrochemical cycling. Second, a thicker Si layer would generate more stress on the membrane during lithium intercalation. This would result in more deflection, which would be easier to detect. However, due to the poor silicon conductivity, thicker films exhibit lower specific capacity, as has been shown experimentally for cells with a planar

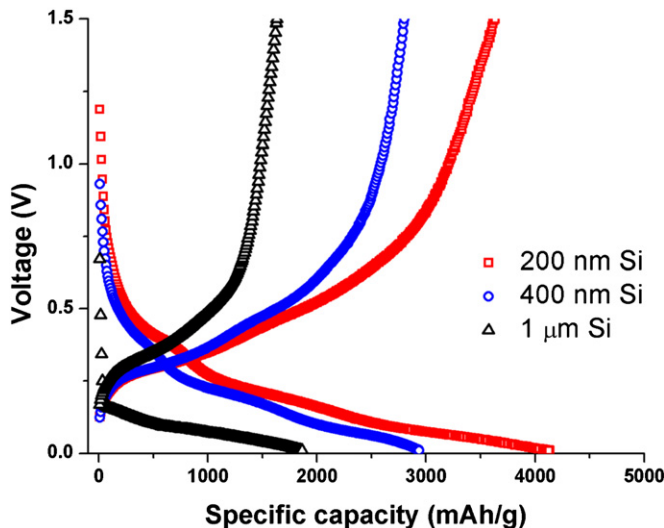


Figure 4. Discharge and charge curves (second cycle) of the cells with planar configuration and different thickness of active silicon layer. Thickness of the Cu current collector layer was fixed at 200 nm in all electrodes. The cells were cycled in the voltage range of 0.01–1.5 V at a current rate of C/2.

electrode configuration (figure 4). Therefore, silicon films thicker than several microns are not applicable for batteries. The thicknesses for the Cu and Si layers of the Fabry–Perot platform were selected based on the results obtained for the cells with planar electrodes configuration.

3. Testing apparatus

The MEMS sensing platform was packaged in a modified coin cell, routinely used in laboratories to test LIB electrodes, as shown in figure 5. To perform optical measurements, a window was machined into the coin cell cap, and double-sided adhesive copper tape (3M) was applied to mount the platform inside the cell. This copper tape creates a hermetic seal of the cell and good electron transport, which are critical conditions for the reliable testing of the LIB electrodes. The battery side of the platform was positioned to face inside the coin cell. The cell was assembled in an argon-filled glove box. A separator soaked in lithium-conducting electrolyte (1 M LiPF₆ solution in ethyl carbonate/diethyl carbonate (EC/DEC, 1:1 by volume)) was placed on top, and metallic lithium was included as the counter electrode to form a lithium half-cell. After cells were closed in the glove box, all experiments were carried out in air under normal ambient conditions.

A photograph of the overall experimental setup is shown in figure 6. The packaged MEMS sensing platform was placed on top of an optical microscope and connected to a battery testing station (Arbin Instruments) controlling lithium intercalation and extraction. Galvanostatic lithium cycling was carried out in the voltage range of 0.01–1.5 V with a current of 40 μ A. During the test, a laser diode emitted red light (660 nm) that shone through the microscope and illuminated the Fabry–Perot cavity. The light was despeckled with a rotating disc. The resulting Fabry–Perot pattern changes, due to deflection of the membrane, were monitored by a CCD camera. The

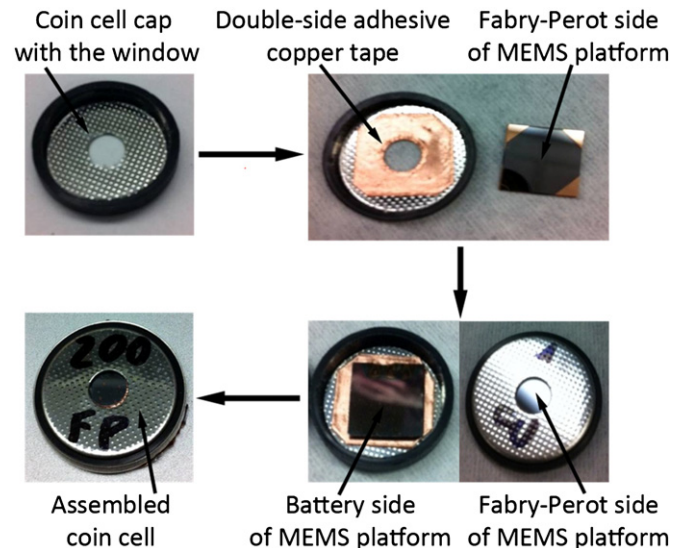


Figure 5. Packaging process of the MEMS sensing platform. A circular window is machined in one half of a coin cell, double-sided adhesive conductive tape is used to mount the device, and the Pyrex surface of the device is visible through the window. Electrolyte, separator and lithium are added inside a glove box and the package is sealed.

experimentally achieved Fabry–Perot pattern is shown on the computer monitor in figure 5. The fringe pattern was recorded as a time-stamped image captured by the camera every 30 s and later correlated with the time-stamped electrochemical data.

4. Results and discussion

It is important to understand how the membranes deflect according to the stress induced by the volume expansion of the active battery material. When the membrane deflection is less than half of the wavelength (<330 nm), membrane displacement cannot be measured by observing fringes. On the other hand, if the membrane deflects more than the Fabry–Perot cavity depth, the membrane will be touching the Pyrex wafer. Therefore, it is worthwhile to simulate the membrane deflection and predict how the fringe pattern will change according to the membrane displacement.

As discussed above, under the simplified assumption that the membrane is a uniform Si₃N₄ layer with 1.0 μ m thickness, membrane deflection due to residual stress of thin films and pre-stress caused by processing conditions (figure 3) should follow the behavior of a circular thin plate with clamped edges under uniform loading (equations (1)–(2)) [15]. When the light source illuminates the Fabry–Perot cavity, incident light is reflected, and the intensity of the reflected light changes according to the shape of the membrane. The reflected light intensity pattern (fringe pattern) change due to membrane deflection can be simulated using Fabry–Perot interferometry principles as described in equation (5) [14]. I_i is the incident light intensity, I_r is the reflected light intensity, F is the finesse of the cavity, and δ is phase difference between each succeeding reflection described in equation (6) where d is the Fabry–Perot cavity depth, n is the refractive index, θ is the

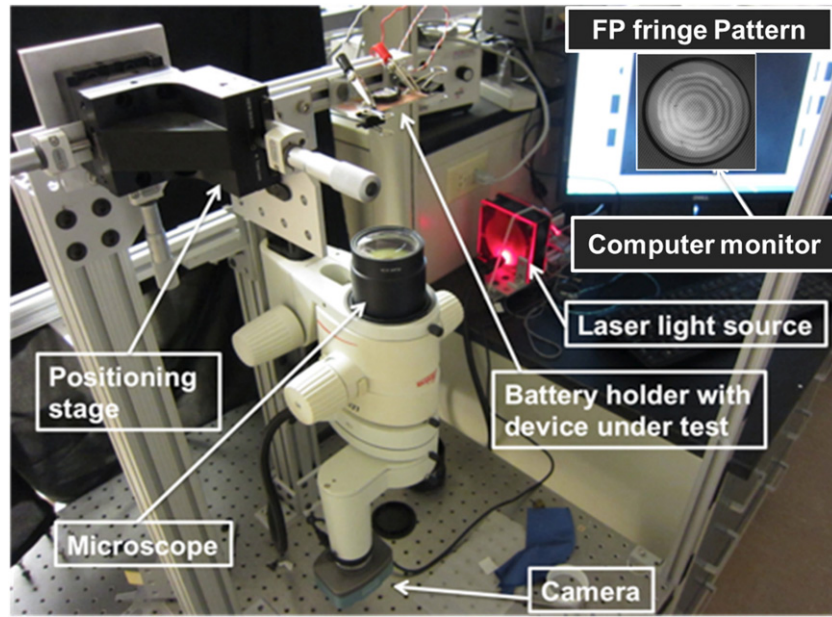


Figure 6. Photograph of the complete experimental setup showing the location of the device under test (face down) relative to the microscope. The red laser light passes through the microscope and illuminates the Fabry–Perot cavity to produce a fringe pattern.

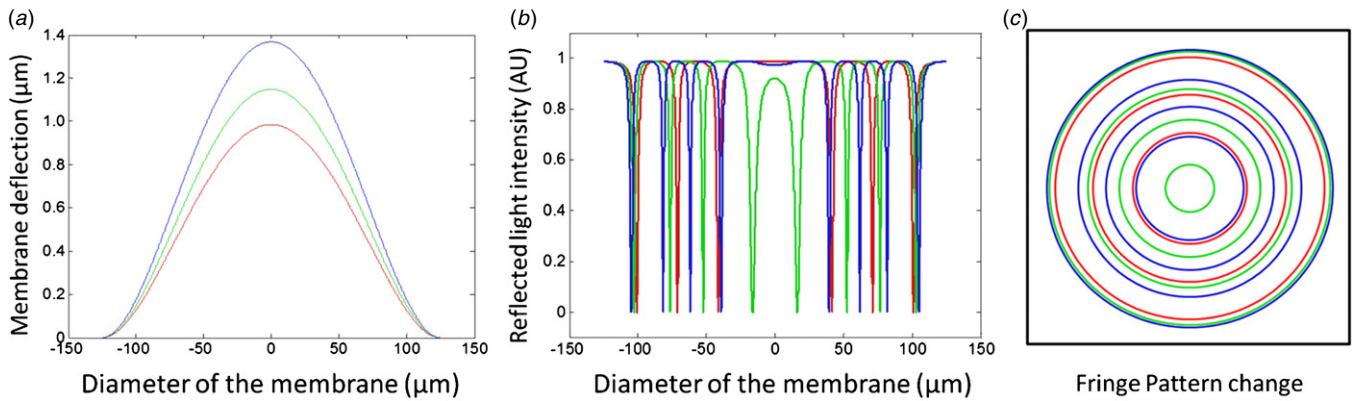


Figure 7. Color-coded diagrams of the calculated results for membrane with residual stress: (a) membrane deflection, (b) intensity change, and (c) FP pattern change. Red, green and blue lines correspond to the applied pressure of 6.85, 7.99 and 9.51 kPa, respectively.

angle of the incident light source, and λ is the wavelength of the light source:

$$I_r = \frac{F \sin^2\left(\frac{\delta}{2}\right)}{1 + F \sin^2\left(\frac{\delta}{2}\right)} I_i \quad (5)$$

$$\delta = \frac{4\pi nd}{\lambda} \cos(\theta). \quad (6)$$

Since the Fabry–Perot cavity depth (d) can be replaced with equation (1), the phase difference δ can be rewritten as equation (7) which enables the reflected light intensity (I_r) to be a function of the membrane radius (r):

$$\delta = \frac{4\pi nW(r)}{\lambda} \cos(\theta). \quad (7)$$

Using equation (1), the shape of the membrane can be simulated using MATLAB (figure 7(a)). Based on different membrane shapes, the interference of light between the lower part of the Fabry–Perot cavity (membrane) and the upper part (Pyrex cover) can also be simulated using equations (5) and (7).

Table 2. Parameters used for simulation of the membrane deflection.

Parameter	Value
Applied pressure (q_0)	6.85, 7.99, and 9.51 kPa
Radius of the membrane (a)	125 μm
Thickness of the Si_3N_4 membrane (h)	1 μm
Flexural rigidity (D) [16]	$2.65 \times 10^{-8} \text{ Pa} \cdot \text{m}^3$
Finesse of the cavity (F)	89.75
Refractive index (n)	1
Angle of the incident light source (θ)	90°
Wavelength of the light source (λ)	660 nm

The intensity is shown in figure 7(b), and the fringe pattern can be constructed (figure 7(c)). The parameters used in this simulation are specified in table 2. This analysis shows that when membrane deflection is positive due to the compressive stress residing in the electrode, the fringe radius becomes bigger which is in good agreement with our experimental results described below.

The cross-section SEM image of the fabricated device (figure 8) shows well-defined Fabry–Perot and battery cavities separated by the membrane. It is critical to control etching of the battery cavity to avoid underetching or overetching. Underetching results in a poor quality, less flexible membrane. Overetching creates notches, which cause non-uniformity in the layers of deposited materials and prevents reliable electrochemical testing.

Since the materials deposition rate can change significantly in the deep battery cavities, the structure of the membrane has been closely inspected. The SEM image (figure 9) shows distinct layers composing the membrane. EDX analysis of the cross-section of membrane (figure 9) revealed that the thickness of Si_3N_4 layer is ca. $1\ \mu\text{m}$. The thickness of the SiO_2 barrier layer is ca. 250 nm, which is in agreement with the value suggested in the platform design. However thickness of Cu current collector (ca. 60 nm) and active Si (ca. 90 nm) layers is significantly below the desired values (250 nm for Cu and 500 nm for Si). This result indicates that, when sputtering is used for materials deposition, the uniform coating of a deep battery cavity cannot be easily achieved. The deposition rate on the membrane should be experimentally re-evaluated in order to enable precise control of the thickness of the materials layers on the ‘battery’ side of the platform. Despite the thin layers of Cu current collector and active Si layer compared to the target thickness, lithium-ion insertion/extraction was confirmed during the electrochemical test. In addition, the thickness of the actual membrane was larger than our preliminary estimates during the design phase ($1.4\ \mu\text{m}$, measured by SEM, figure 9). This thicker membrane would result in smaller deflection of the membrane and would not be a problem with the chosen Fabry–Perot cavity depth.

Changes in the Fabry–Perot interference pattern occur over long time scales, where a single battery cycle may take several hours. Measurements over numerous cycles can produce thousands of images taken many days apart. To analyze the data, computerized image processing is necessary to handle the information. After time-stamped image capture, the image stack is preprocessed (e.g. intensity normalization and registration correction) and analyzed in MATLAB. The algorithm is schematically illustrated in figure 10. Since the observed phenomenon is radially symmetric, the image data is converted from Cartesian (x, y) to polar (r, θ) coordinates. The angle (θ) information for a constant radius (r) is averaged together to produce a plot of light intensity as a function of radial distance from the center of the image. This effectively oversamples the fringe position by combining independent measurements of its position, each at different angle from the center of the image. Next, two features are algorithmically detected from the intensity plot: (1) one of the moving fringes is detected as the local minima closest to the center of the image at the start of the experiment, and (2) the edge of the cavity is identified as the local minima with highest radial distance. The tracking algorithm looks for the moving fringe near the last known position over the course of the experiment. The individual fringes do not move significantly in 30 s, therefore the fringe position can be reliably tracked over several days. Finally, the moving fringe position can be measured relative

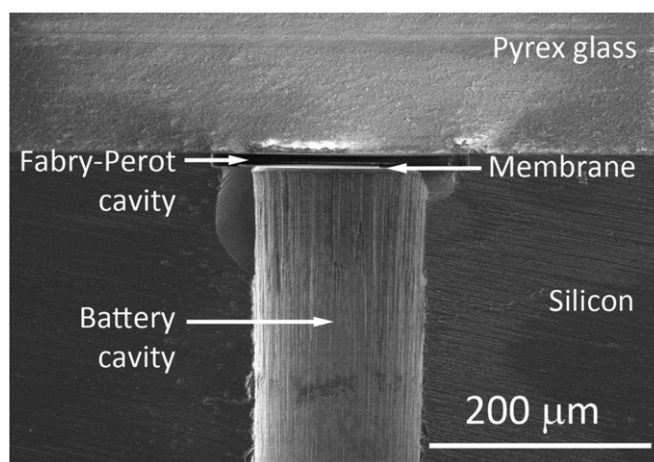


Figure 8. Cross-section SEM image of the membrane in the MEMS platform.

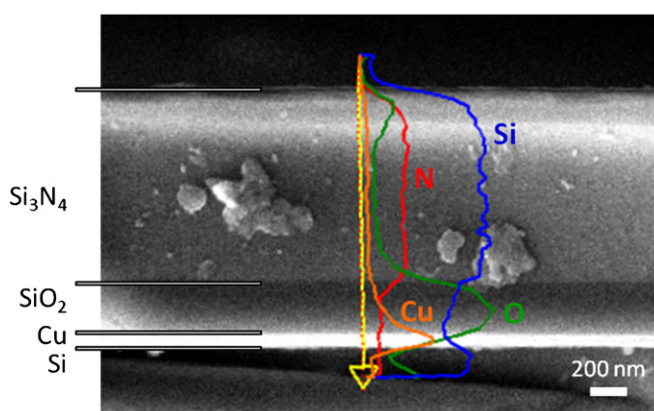


Figure 9. Cross-section SEM image of the materials stack composing the membrane combined with EDX line scan elemental mapping indicating Si, N, O, and Cu elemental profiles. The upper section of the membrane is silicon nitride, followed by silicon oxide, with a copper current collector on the bottom. The sidewall of the cavity is visible in the lower background of the image.

to the immovable edge of the cavity in order to prevent drift in the position of the sample from affecting fringe position measurements. It is then plotted as a function of time where the measurement at $t = 0$ (pristine electrode) is defined as zero measured shift (figure 11(a)).

The correlation between electrochemical data and change in Fabry–Perot fringe radius (fringe shift) for a membrane with $250\ \mu\text{m}$ diameter during the second electrochemical cycle is shown in figure 11(b). No change in the monitored fringe radius means zero fringe shift, and a larger fringe radius is indicated by a more negative fringe shift number. Although the fringe shift is measured in arbitrary units (AU) it is plotted in a way that is believed to be related to the compressive stress generated in the silicon anode [8]; a more negative fringe shift corresponds to a more compressive film stress. Upon lithium intercalation, the fringe radius initially increases significantly, and then it remains constant until the charge starts. On charge, the same trend occurs in the opposite direction: first, fringe radius significantly decreases, and then it remains relatively constant until the end of the cycle.

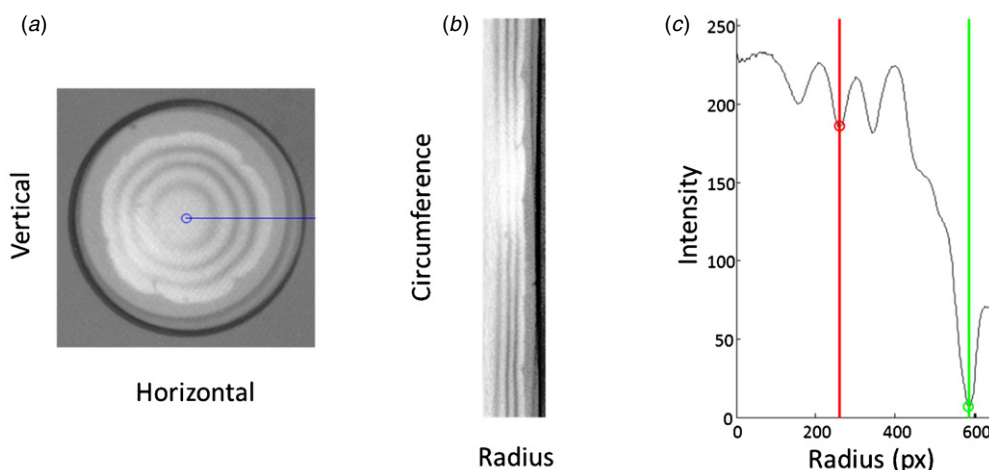


Figure 10. Fringe shift measurement algorithm: (a) photograph of experimentally obtained fringe pattern in Cartesian coordinate system, (b) experimentally obtained fringe pattern converted from Cartesian to polar coordinates and (c) plot of light intensity as a function of radial distance from the center of the image. The vertical green line on the right indicates the unmoving edge of the membrane, and the vertical red line on the left indicates the tracked position of the moving fringe.

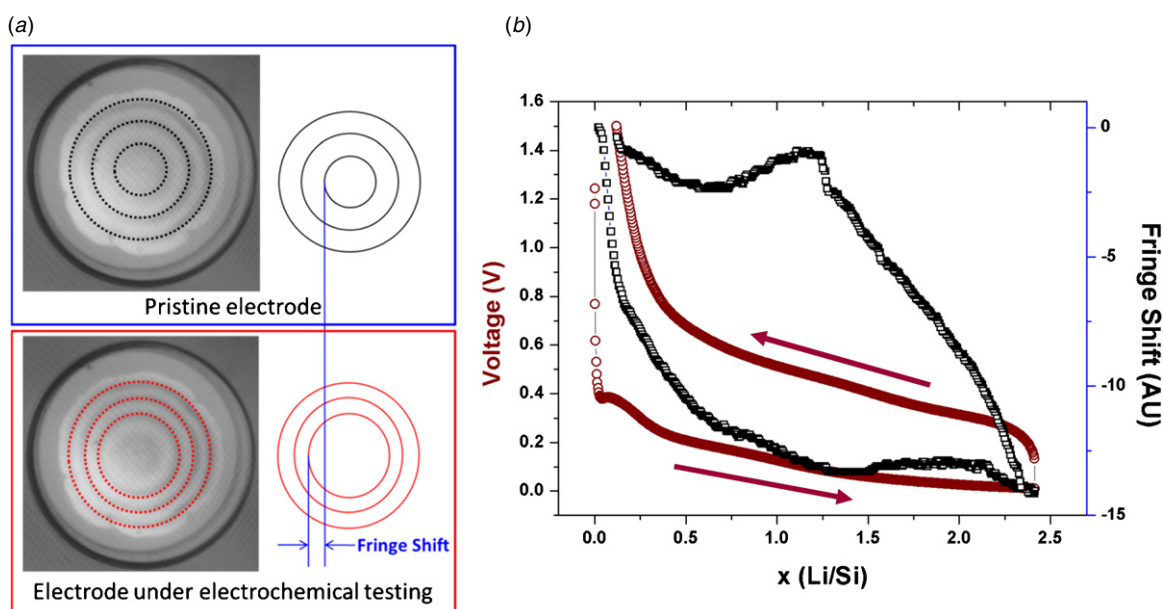


Figure 11. (a) Photographs of experimentally obtained fringe patterns and corresponding diagram for ‘fringe shift’. (b) Correlation between Fabry–Perot fringe radius change and electrochemical cycling of thin-film silicon electrode as a function of lithium intercalation degree. The red line (circles) corresponds to the electrochemical discharge/charge curve, and the black line (squares) indicates corresponding fringe shift. The arrows indicate cycling directions.

To evaluate the mechanical response of the membrane itself, a pneumatic test was conducted in the same membrane deflection range using a new device with membrane radius ($125\ \mu\text{m}$) similar to that of the electrochemical test. According to the experimental result, a minimum of three and a maximum of four fringes were observed during the electrochemical test. Each fringe appears when deflection of the membrane is equal to half of the wavelength ($330\ \text{nm}$). Therefore, in the present experiment the membrane deflected from 990 to $1320\ \text{nm}$. As a result, it is not possible for the membrane to be mechanically constrained by the Pyrex glass cover that is $12\ \mu\text{m}$ away.

It is also possible that there might be significant nonlinearity in the measurement technique. The membrane deformation could then become unresponsive to changes in

lithium intercalation at some point. In order to investigate the linearity, a pneumatic test was performed since it is non-destructive and the applied pneumatic pressure will be linearly related to the stress in the membrane (equation (3)). In this device, the membrane consisted of Si_3N_4 ($1\ \mu\text{m}$) and SiO_2 ($250\ \text{nm}$) layers. The overall experimental setup for pneumatic test is shown in figure 12(a). The applied pressure was carefully controlled by using a pressure regulator and flow control upstream of the device under test; a bleeder valve was used to slowly change the pressure from an initial value. The pressure was delivered using a custom acrylic plate with multiple ports (one for applied pressure and one for the pressure monitor) and a small hole that interfaced to the battery cavity. Another acrylic plate was used to cover

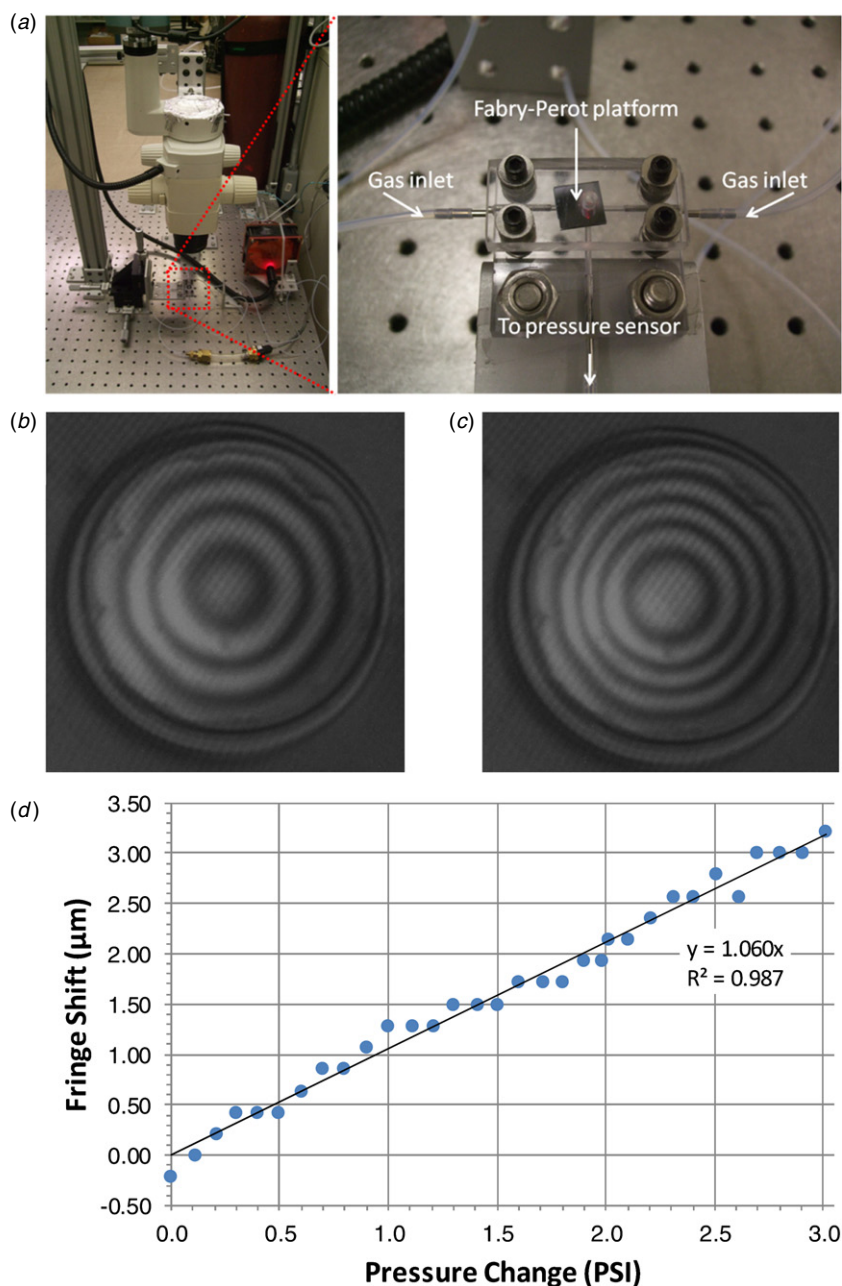


Figure 12. Pneumatic test: (a) overall experimental setup, (b)–(c) photographs of experimentally obtained fringe patterns with three and four fringes, and (d) correlation between fringe shift and linearly varying pressure applied on the membrane.

the top of the device and was bolted to the bottom plate; this securely sealed the device in place. The applied pressure was monitored using the voltage output from a pressure transducer (OMEGA Engineering Inc., PX181B-100G5V), a benchtop regulated power supply (HP 6214c) and a 6.5-digit benchtop multimeter (Keithly 2000-20) with MX+B scaling capability. A resolution of 0.1 mV was obtained, corresponding 0.005 PSI resolution with this setup. After adjusting the pressure to a nominal value to induce a pattern of four fringes, the pressure was changed in 0.1 PSI increments and an image of the fringe patterns were captured (figures 12(b) and (c)). The images were analyzed using the same algorithm to produce a plot of fringe shift versus pressure change. The result is shown in figure 12(d). According to our test

result, fringe shift varies linearly with applied pressure and nonlinearities are below our capability to measure, which is limited by the pixel resolution of the image capture of the fringe patterns. Based on these results, the fringe shift is expected to be linearly proportional to the stress residing in the membrane over the reported measurement range. Therefore, the constant fringe shift observed during both charge and discharge cycles (figure 11) is related to the mechanical properties of electrochemically active silicon and not caused by deformation limitations of the membrane.

Therefore, the electrochemical test results are in good agreement with previously reported data for thin-film silicon electrodes [8, 12]. Upon lithium intercalation the silicon film initially deforms elastically, resulting in rapid increase

of the Fabry–Perot fringe radius. This is followed by lithiated silicon deforming plastically under compressive stress, which corresponds to the constant Fabry–Perot fringe radius. Upon lithium extraction, the electrode first undergoes elastic straining in the opposite direction (decrease of Fabry–Perot fringe radius) leading to a tensile stress; subsequently it deforms plastically during the rest of the charge. This result indicates that the developed MEMS platform combined with reliable packaging scheme is capable of *in situ* characterization of electrochemically induced stress/strain in various thin-film LIB electrodes. This study is essential for the development of new generation LIB electrodes with long-term reliable and stable electrochemical performance.

5. Conclusions

In this work the sensing capabilities of a MEMS Fabry–Perot membrane-based platform have been demonstrated for the first time for *in situ* characterization of electrochemically induced stress/strain in thin-film LIB electrodes. The membrane deflection is induced by silicon thin-film electrode volume expansion/contraction during electrochemical cycling. This sensing technology enables *in situ* characterization of various thin-film LIB electrodes and leads to a better understanding of electrochemically driven stress generation, deformation and fracture causing degradation and failure of batteries. The results from electrochemical cycling of LIB materials show a sensitive and robust measurement methodology that can be extended to numerical measurements of mechanical properties. A model of membrane deflection will be developed during the next phase of this research to achieve this goal.

Acknowledgments

This work was supported by the Nanostructures for Electrical Energy Storage, an Energy Frontier Research Center funded by the U.S. Department of Energy (DOE), Office of Science, Office, Basic Energy Sciences (BES), under award number DESC0001160. The authors acknowledge the staff at Maryland Nanocenter.

References

- [1] Tarascon J M and Armand M 2001 Issues and challenges facing rechargeable lithium batteries *Nature* **414** 359–67
- [2] Besenhard J O, Komenda P, Paxinos A, Wudy E and Josowicz M 1986 Binary and ternary Li-alloys as anode materials in rechargeable organic electrolyte Li-batteries *Solid State Ion.* **18–9** 823–7
- [3] Wang J, Raistrick I D and Huggins R A 1986 Behavior of some binary lithium alloys as negative electrodes in organic solvent-based electrolytes *J. Electrochem. Soc.* **133** 457–60
- [4] Li J, Dozier A K, Li Y, Yang F and Cheng Y-T 2011 Crack pattern formation in thin film lithium-ion battery electrodes *J. Electrochem. Soc.* **158** A689–94
- [5] Teki R, Datta M K, Krishnan R, Parker T C, Lu T-M, Kumta P N and Koratkar N 2009 Nanostructured silicon anodes for lithium ion rechargeable batteries *Small* **5** 2236–42
- [6] Hertzberg B, Benson J and Yushin G 2011 *Ex-situ* depth-sensing indentation measurements of electrochemically produced Si–Li alloy films *Electrochem. Commun.* **13** 818–21
- [7] Chon M J, Sethuraman V A, McCormick A, Srinivasan V and Guduru P R 2011 Real-time measurement of stress and damage evolution during initial lithiation of crystalline silicon *Phys. Rev. Lett.* **107** 045503
- [8] Sethuraman V A, Chon M J, Shimshak M, Srinivasan V and Guduru P R 2010 *In situ* measurements of stress evolution in silicon thin films during electrochemical lithiation and delithiation *J. Power Sources* **195** 5062–6
- [9] Sethuraman V A, Chon M J, Shimshak M, Van Winkle N and Guduru P R 2010 *In situ* measurement of biaxial modulus of Si anode for Li-ion batteries *Electrochem. Commun.* **12** 1614–7
- [10] Sethuraman V A, Srinivasan V, Bower A F and Guduru P R 2010 *In situ* measurements of stress-potential coupling in lithiated silicon *J. Electrochem. Soc.* **157** A1253–61
- [11] Soni S K, Sheldon B W, Xiao X C, Bower A F and Verbrugge M W 2012 Diffusion mediated lithiation stresses in Si thin film electrodes *J. Electrochem. Soc.* **159** A1520–7
- [12] Soni S K, Sheldon B W, Xiao X C and Tokranov A 2011 Thickness effects on the lithiation of amorphous silicon thin films *Scr. Mater.* **64** 307–10
- [13] Soni S K, Sheldon B W, Xiao X C, Verbrugge M W, Ahn D, Haftbaradaran H and Gao H J 2012 Stress mitigation during the lithiation of patterned amorphous Si islands *J. Electrochem. Soc.* **159** A38–43
- [14] Hernandez G 1986 *Fabry-Perot Interferometers* (New York: Cambridge University Press)
- [15] Timoshenko S P and Woinowsky-Krieger S 1964 *Theory of Plates and Shells* (New York: McGraw-Hill)
- [16] Gavan K B, Westra H J R, van der Drift E W J M, Venstra W J and van der Zant H S J 2009 Size-dependent effective Young's modulus of silicon nitride cantilevers *Appl. Phys. Lett.* **94** 233108